

Journal of the Pakistan Institute of Chemical Engineers



Journal homepage: www.piche.org.pk/journals

DOI: https://doi.org/10.54693/piche.05224



Effect of Grit Blasting on Electrochemical Behavior of Hydroxyapatite Coated AZ31B Magnesium Alloy

F. Hussain^{1*}, M. U. Manzoor¹, M. Kamran¹, T. Ahmad¹, F. Riaz¹, M. Ishtiaq¹, M. Shakeel² Submitted: 18/08/2024, Accepted: 20/12/2024, Published: 24/12/2024

Abstract

Magnesium (Mg) alloys have garnered considerable interest as biodegradable materials for bone fixation implants. In this study, AZ31B Mg alloy substrates were grit-blasted with quartz and alumina particles at varying pressures and subsequently coated with hydroxyapatite via electrodeposition for different durations. Scanning electron microscopy was employed to examine the surface morphology of the hydroxyapatite layer, while potentiodynamic polarization and electrochemical impedance spectroscopy were conducted to assess the layer's nature, coverage, and effectiveness in a simulated body fluid. The findings indicate that longer deposition times led to increased surface coverage. Notably, a capacitive hydroxyapatite layer with a dense inner structure and complete surface coverage was achieved after 40 minutes of deposition on quartz- and alumina-blasted samples at a blasting pressure of 1000 kPa. The findings of this study aid in developing biocompatible coatings on magnesium alloys for bone fixation implants.

Keywords: Mg Alloy, Grit Blasting, Blasting Pressure, Hydroxyapatite Coating, potentiodynamic polarization, electrochemical impedance spectroscopy

1. Introduction:

An uncontrollable increase in population leads to Biodegradable magnesium (Mg) alloys have attracted significant attention as metallic bone fixation implants due to their lower density, elastic modulus comparable to that of natural bone, excellent mechanical properties, and low toxicity [1-7]. The human body can progressively eliminate the released Mg ions through urine and sweating without causing any harmful effects [8-10]. However, a significant drawback associated with Mg alloys is their accelerated degradation rate, which leads to premature implant failure before the completion of bone healing [11]. The performance of implants is

adversely affected by this degradation, which limits their clinical usability as load-bearing implants [12,13]. Several approaches have been considered to reduce the degradation rate, such as alloying, surface modification, and coatings [14-17]. The process of alloying presents a feasible approach to improve the corrosion resistance of Mg in body fluids. However, upon dissolution of the Mg alloy, the alloying elements will also undergo absorption inside the human body. Therefore, the addition of elements such as Zr, Al, Ce, Pr, and Y into Mg alloys is limited due to their inherent toxicity [18-21]. Another feasible approach is the surface modification of Mg alloys [22]. The application of a bioactive coating onto the surface of Mg alloys has also been identified as an

Corresponding Author: Faraz Hussain (faraz.imme@pu.edu.pk)

Institute of Metallurgy & Materials Engineering, University of the Punjab, Lahore Institute of Advanced Materials, Bahauddin Zakariya University (BZU), Multan, Pakistan

effective approach to improve the corrosion resistance [23]. The application of hydroxyapatite (HA) coating based on calcium phosphorous (Ca-P) is a widely used bioactive coating for Mg alloys. This coating functions as a protective barrier and promotes the growth of natural bone cells. Its primary purpose is to regulate the corrosion kinetics of these alloys [24-25]. Several approaches have been documented in the literature about the deposition of HA coating on Mg alloys including chemical conversion techniques, sol-gel processes, electrodeposition, hydrothermal, and microarc oxidation processes [26-30]. Among these approaches, electrodeposition has received significant attention due to its cost-effectiveness, versatility, and ability to regulate the thickness and chemical composition of HA by adjusting the deposition conditions.

The effects of electrolyte composition, potential, pH, temperature, and current density on HA-coating developed by the electrodeposition approach on Mg alloys have been studied by many researchers [31-36]. However, the effect of surface roughness on the

electrochemical behavior of electrodeposited HAcoating on Mg alloys has not been published as far as we know. From this perspective, the main focus of this research is to investigate the effect of surface roughness on the corrosion behavior of electrodeposited HA-coating on Mg alloys in simulated body fluid (SBF).

2. Material and methods:

2.1 Grit Blasting Operation

AZ31B Mg alloy samples were selected as a substrate for grit blasting operation. The grit blasting procedure was conducted by using a special pressure blasting system. The system comprised an abrasive container, a blasting gun, a sample holder and an air compressor. Particles of abrasive material were drawn into the blasting gun and pushed through it by means of compressed air. A nozzle angled at 90° to the sample surface directed the abrasive particles in the desired direction [37]. The grit blasting parameters that were selected for current study are listed in Table 1.

Table 1: Grit Blasting Operation Parameters

Abrasive Type	Abrasive Size (mesh)	Blasting Pressure (psi)	Blasting Angle (θ)	Blasting Distance (mm)	Blasting Time (seconds)
Alumina	<200 µm	350, 700, 1000	90	10	20
Quartz	<200 μm	350, 700, 1000	90	10	20

2.2 Electrochemical Deposition of HA Coating:

The surface of the substrate was subsequently coated with HA by an electrochemical technique.

The electrolyte solution used for HA coating is listed in Table 2.

Table 2: Electrolyte Solution for HA Coating

Substance	Ca(NO ₃) ₂	NH ₄ H ₂ PO ₄	NaNO ₃	H ₂ O ₂	Deionized Water
Amount	2.8 g	1.16 g	3.4 g	8 ml	392 ml

The electrodeposition process was carried out using a Potentiostat (Gamry Interface 1000E) with a three-electrode system. The counter electrode consisted of a graphite rod, the reference electrode was a saturated KCI solution of Ag/AgCI, and the working electrode was a grit-blasted AZ31B Mg alloy specimen. The electrodeposition procedure was carried out at room temperature for 10, 20, 30, and 40 minutes with an applied potential of -1.4V. The coating deposition process used a magnetic stirrer to keep the electrolytic

solution homogeneous and consistent. The samples were then immersed in a 0.25 M NaOH solution for 2 hours at 60 °C. As a result, the HA coating was developed on the grit-blasted samples. Afterward, the samples were washed in deionized water and dried for 2 to 3 hours [38]. Scanning electron microscopy (SEM, FEI Inspect S50) was utilized to analyze the surface morphology of the electrodeposited HA coating. The labeling of the samples to identify the process parameters is provided in Table 3.

Table 3: Labelling of Samples

Sample Labelling	Description
PS	Pristine Sample
A350, A700, A1000	Alumina blasted samples at 350,700 and 1000 kPa
Q350, Q700, Q1000	Quartz blasted samples at 350,700 and 1000 kPa
HA10, HA20, HA30, HA40	Deposition time of 10, 20, 30 and 40 minutes

2.3. Electrochemical Testing:

Potentiodynamic polarization (PD) and Electrochemical impedance spectroscopy (EIS) techniques were used to investigate the electrochemical behavior of electrodeposited HA-coated samples pre-blasted with quartz and alumina particles at different blasting pressures. The exposed sample area was 1 cm2. A three-electrode configuration was utilized in the electrochemical investigations, consisting of a working electrode (sample), a reference electrode (Ag/AgCl saturated KCl), and a counter electrode (graphite

electrode). The electrolyte used was a solution of Ringer's lactate kept at 37 °C. The PD measurements were performed by applying a potential range of -0.5 to +1.5 V, with a scan rate of 5 mV/s. EIS was performed with an AC amplitude of ±10 mV(rms) with a test frequency ranging from 105 to 10-2 Hz.

3. Results and Discussion:

3.1 Surface Morphology:

The SEM image of the untreated pristine sample, depicted in Fig. 1(a), exhibits surface scratches resulting from the rolling process.

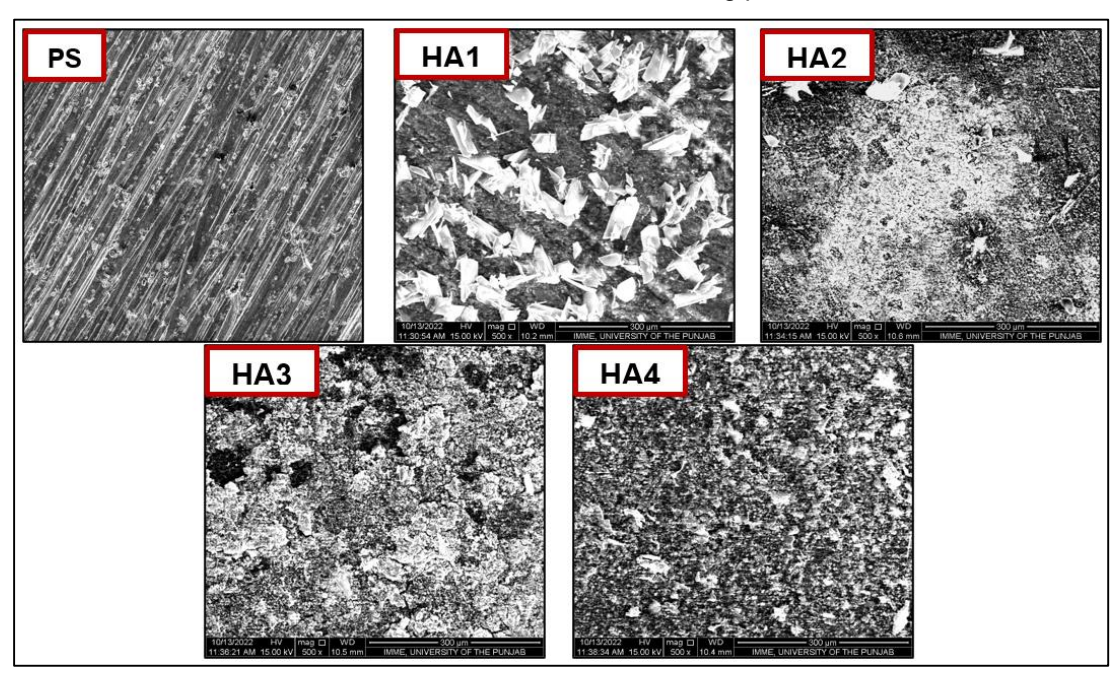


Figure 1: SEM Micrographs of Pristine Samples with Different HA Deposition Times

The surface morphology showing the HA-coating treatment time of 10 minutes on the pristine sample is displayed in Fig. 1(b), and it is evident that a flake-like HA layer was formed exhibiting partial surface coverage. However, when the coating deposition period increases from 10 to 20 minutes, there is a significant change in the coating morphology, resulting in a fine structure with considerable surface coverage, as depicted in Fig. 1(c). As the coating deposition period increased from 20 to 30 and to 40 minutes, the coating

morphology gradually became coarser, resulting in full surface coverage (about 75%), as demonstrated in Figs. 1(d-e). The SEM images of both untreated and quartz blasted samples are depicted in Fig. 2. The surface morphology of the quartz blasted sample with 350 kPa blasting pressure is displayed in Fig. 2(a). The images of the quartz blasted samples coated with HA at different deposition times are demonstrated in Figs. 2(b-e). It can be shown from the surface morphology of the HA-coating on quartz blasted sample for a

treatment time of 10 minutes as illustrated in Fig. 2(b) that a large flake-type HA-coating layer was developed with partial surface coverage. As the coating deposition

time increased from 10 to 20 minutes, the coating morphology remains unchanged, resulting in maximum surface coverage, as depicted in Fig. 2(c).

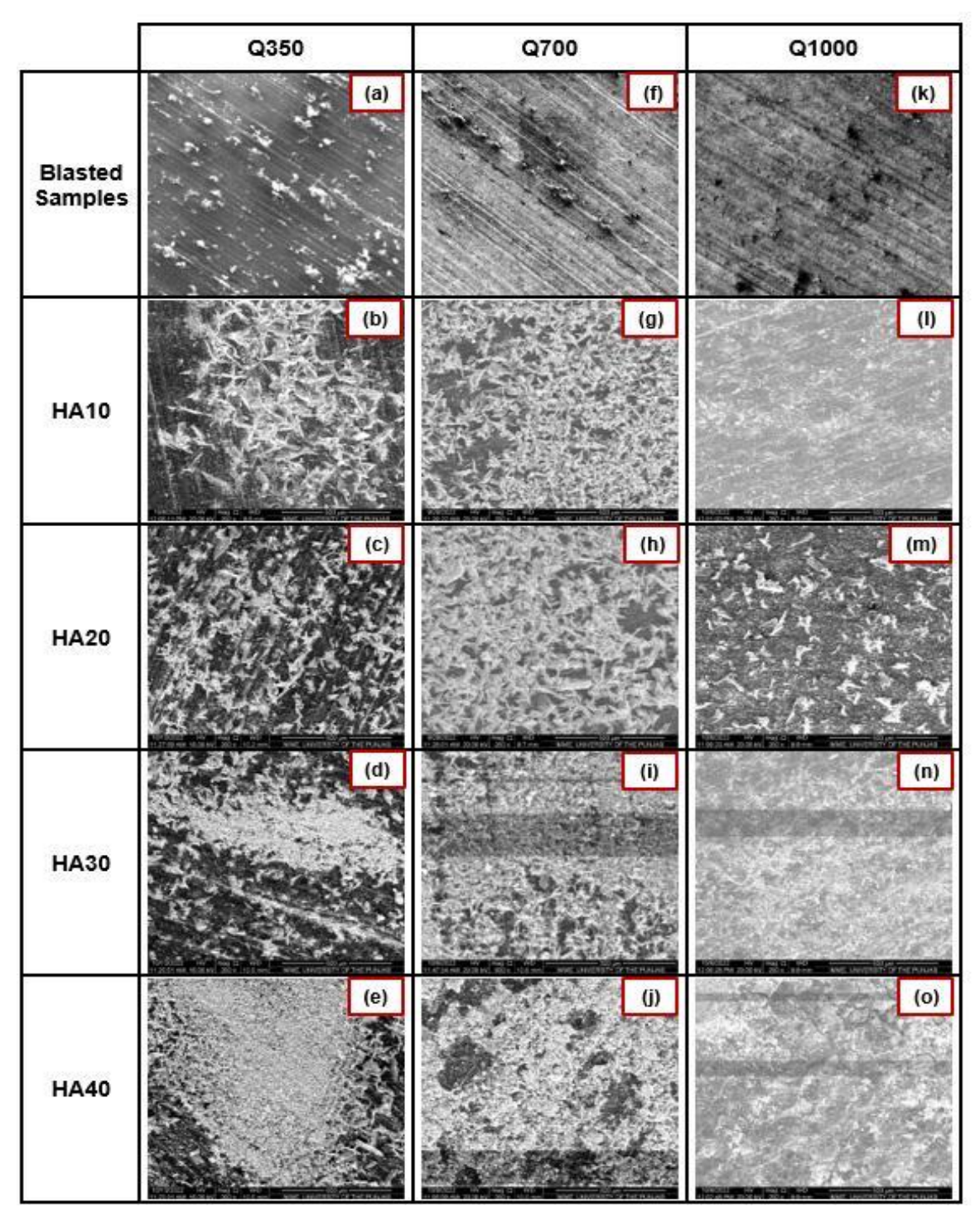


Figure 2: SEM Micrographs of Quartz Blasted Samples with Different HA Deposition Times

When the coating deposition time was increased from 20 to 30 and to 40 minutes, there was a gradual coarsening of the coating morphology and a change in surface coverage from maximum to full, as depicted in Figs. 2(d-e) respectively. The SEM image of the quartz blasted sample with 700 kPa blasting pressure is

displayed in Fig. 2(f). The surface morphologies of HA-coated quartz blasted samples with 700 kPa blasting pressure is depicted in Figs. 2(g-j). It is evident that the HA-coating treatment retains a flake-like appearance with a coarse crystal structure after a time of 10 minutes, effectively covering the maximum sample surface. The

coarsening of the HA layer is observed as the treatment time increases up to 40 minutes. The surface morphology of the quartz blasted sample with 1000 kPa blasting pressure is depicted in Fig. 2(k). The coating morphology of quartz blasted samples with 1000 kPa blasting pressure demonstrated complete surface coverage for all HA coating durations as depicted in Figs. 2(I-o). A coating morphology characterized by a fine structure and full surface coverage was developed. The initiation of cracks was observed only after a deposition time of 40 minutes at a blasting pressure of 350 kPa. These cracks became more obvious in the samples subjected to blasting at a pressure of 1000 kPa. This phenomenon can be attributed to the increased internal stresses within the thicker coating layer. However, all of the blasted samples demonstrated an increase in coating fineness as processing time increased.

The SEM images of untreated and treated alumina blasted samples are depicted in Fig. 3. The surface morphology of the alumina blasted sample with 350 kPa blasting pressure is displayed in Fig. 3(a). The SEM images of the HA-coating with different deposition times on alumina blasted samples with 350 kPa blasting pressure are illustrated in Figs. 3(b-e). The surface morphologies of the HA-coating on alumina blasted sample, for processing time of 10 and 20 minutes, as depicted in Figs. 3(b-c), shows that at 350 kPa blasting pressure and coating deposition time of 10 and 20 minutes, few flake-type **HA-coating** layers with partial surface coverage are seen, as evidenced by the presence of visible base metal scratches on the surface. However, as the coating deposition time increased from 20 to 30 and to 40 minutes, the coating morphology exhibited a gradual coarsening, and a complete surface covering was observed, as depicted in Figs 3(d-e) respectively. The surface morphology of the alumina blasted sample with 700 kPa blasting pressure is depicted in Fig. 3(f). It can be observed that the HA treatment at 10 minutes has a flake-like appearance, characterized by a coarse crystal structure, and effectively covers the maximum sample surface. The surface morphology changes from a coarse to a fine layer of HA with an increase in treatment time to 40 minutes. The SEM image of the alumina blasted sample with 1000 kPa blasting pressure is depicted in Fig. 3(k). It can be observed that the HA behavior of alumina blasted samples with 1000 kPa blasting pressure demonstrates complete surface coverage for all HA times. The coating morphology exhibited a significant change, resulting in a fine structure that achieved full surface coverage after a deposition period of 40 minutes at a blasting pressure of 1000 kPa. The formation of cracks appears to be more noticeable when the deposition period increases to 40 minutes at a blasting pressure of 1000 kPa, compared to the 350 kPa and 700 kPa blasting pressures where the thickness of the HAcoating layer increased. This finding confirms the assumption that cracks develop as a result of internal stresses when the thickness of the HA layer is beyond a certain limit.

3.2. Potentiodynamic Polarization Scan:

The PD curves of pristine samples electrodeposited with HA for varying durations in SBF solution are shown in Fig. 4(a). Similarly, the PD curves of pre-blasted samples with quartz and alumina particles at different blasting pressures, electrodeposited with HA for varying durations in SBF solution are shown in Figs. 4 and 5 respectively.

Tafel extrapolation incorporating the linear portion was applied to the PD scans using Gamry E-Chem Analyst software to determine the corrosion current density (I_{corr}), corrosion potential (E_{corr}), and corrosion rate values. Similarly, the polarization resistance (R_p) was calculated by the formula as given in Eq. 1 [38]:

$$R_{p} = \frac{\beta_{a}\beta_{c}}{2.303I_{corr}(\beta_{a}+\beta_{c})} \tag{1}$$

Here, βa and βc are the anodic and cathodic Tafel slopes.

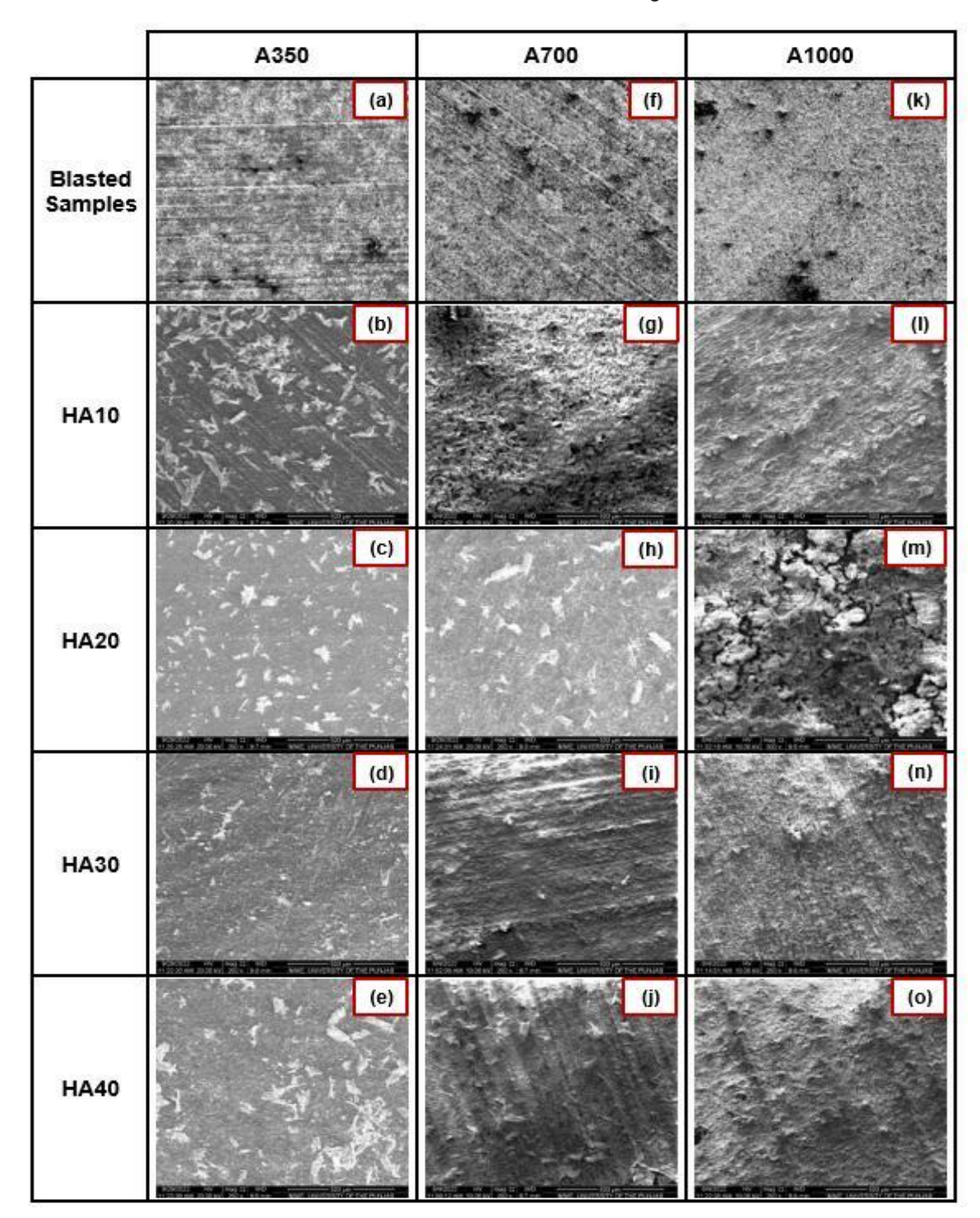


Figure 3: SEM Micrographs of Alumina Blasted Samples with Different HA Deposition Times

The corrosion current density (I_{corr}), corrosion potential (E_{corr}), corrosion rate and polarization resistance (R_p) data are shown in Tables 4-6.

In a potentiodynamic scan, the anodic polarization curve indicates the behavior of metal dissolution i.e. corrosion reaction as given in Eq. 2

$$Mg = Mg^{2+} + 2e^{-} \text{ or } Mg_{(s)} + 2(OH)^{-} = Mg(OH)_{2(s)} + 2e^{-}$$
 (2)

while cathodic polarization curve reveals evolution of hydrogen as given in Eq. 3 [39].

$$2H_2O + 2e^- = 2(OH)^- + H_2 \text{ or } 2H^+ + 2e^- = H_{2(g)}$$
 (3)

More positive E_{corr}, relatively lower I_{corr}, and higher R_p values indicate good corrosion resistance [37]. The cathodic polarization curves of pristine samples electrodeposited with HA exhibit a linear

trend throughout the polarization range. In contrast, the anodic polarization curves of pristine samples electrodeposited with HA indicate a progressive shift

increase in the deposition time of HA is associated with

towards passivation behavior as shown in Fig. 4. An

. ...

a major shift of E_{corr} values towards positive potential and a significant decrease in I_{corr} values and corrosion rates, as reported in Table 4.

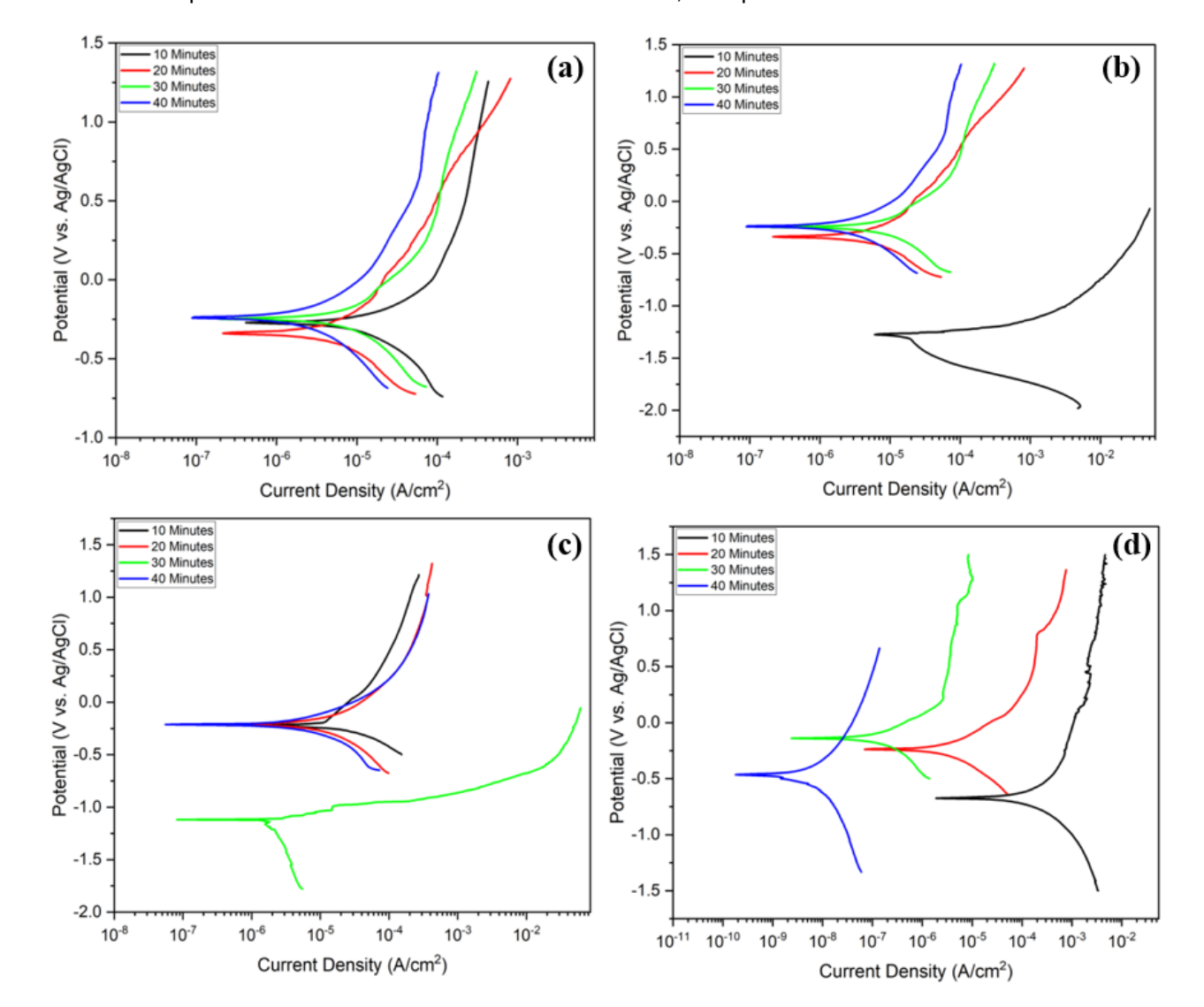


Figure 4: PD curves with different HA deposition times in SBF for (a) Pristine samples (b) Quartz blasted samples at 350 kPa blasting pressure (c) Quartz blasted samples at 700 kPa blasting pressure (d) Quartz blasted samples at 1000 kPa blasting pressure

Table 4: Electrochemical Parameters selected for corrosion testing of Pristine sample

	Electrod	hemical Parameters	
E _{corr} (mV)	I _{corr} (μΑ/cm²)	Corrosion Rate (mpy)	R _p (KΩcm²)
-289.9	21.451	32.03	2.51
-318.6	4.608	6.5	14.39
-244.6	0.765	1.672	69.71
-235.6	0.088	0.345	696.26
	-289.9 -318.6 -244.6	E _{corr} (mV) I _{corr} (μA/cm²) -289.9 21.451 -318.6 4.608 -244.6 0.765	E _{corr} (mV) I _{corr} (μΑ/cm²) Corrosion Rate (mpy) -289.9 21.451 32.03 -318.6 4.608 6.5 -244.6 0.765 1.672

that the values of I_{corr} decreased from 15.518 to 0.030 $\mu A/cm^2$ and E_{corr} shifted from -1295.6 V to -1257.1 V with an increase in HA deposition time from 10 minutes to 40

minutes for quartz blasted samples.

Table 5: Electrochemical parameters selected for corrosion testing of Quartz blasted samples

		Electroc	hemical Parameters	
Sample	E _{corr} (mV)	I _{corr} (μΑ/cm²)	Corrosion Rate (mpy)	R _p (KΩcm²)
Q350-HA10	-1295.6	15.518	22.7	3.91
Q350-HA20	-1049.1	1.708	3.1	39.98
Q350-HA30	-60.8	0.654	0.982	128.57
Q350-HA40	-1257.1	0.030	0.117	2086.70
Q700-HA10	-226.6	10.067	16.5	4.27
Q700-HA20	-213.0	0.729	2.3	57.06
Q700-HA30	-1156.6	0.318	0.673	188.69
Q700-HA40	-198.4	0.013	0.056	3918.08
Q1000-HA10	-673.8	8.429	11.4	6.09
Q1000-HA20	-239.7	0.494	1.493	87.94
Q1000-HA30	-135.9	0.180	0.144	336.39
Q1000-HA40	-468.8	0.008	0.028	5126.14

The near zero value of Icorr confirms the complete coverage in Q350-HA40 sample (0.030 µA/cm²) compared to Q350-HA10 sample (15.518 µA/cm²). A 194-fold decrease in corrosion rate from 22.7 mpy to 0.117 mpy with an increase in HA deposition time indicates the effectiveness of the HA coating. Similarly, the R_p values show a 533-fold increase in polarization resistance from 3.91 to 2086.70 KΩcm², confirming the resistance behavior of the HA coating. The values of Icorr decreased from 10.067 to 0.013 µA/cm² and E_{corr} shifted from -226.6 V to -198.4 V with an increase in the HA deposition period. The near-to-zero value of Icorr confirms the complete coverage in Q700-HA40 sample having a measured corrosion density of 0.013 µA/cm² compared Q700-HA10 sample to (10.067)µA/cm²). Likewise, the corrosion rates of these samples exhibit a significant reduction of 295-fold, from 16.5 to 0.056 mpy, as the anodization period increases, which clearly proves the efficiency of the HA layer. A 918-fold increase in polarization resistance, ranging from 4.27 to 3918.08 KΩcm² confirms the resistance characteristics of the HA layer. The values of Icorr decreased from 8.429 to 0.008 µA/cm² and E_{corr} shifted from -673.8 V to -468.8 with an increase in the HA deposition duration. The near zero value of Icorr indicates that Q1000-HA40 sample has achieved full coverage, as evidenced bγ the measured corrosion density of 0.008 µA/cm² compared to Q1000-HA10 sample (8.429 µA/cm²). A 407-fold decrease in corrosion rate from 11.4 to 0.028 mpy with an increase in the HA deposition period demonstrates that the coating becomes more effective. Similarly, the Rp values show a 842-fold increase in polarization resistance from 6.09 to 5126.14 KΩcm² confirming the resistive behavior of the coating.

The anodic and cathodic polarization curves of electrodeposited HA samples pre-blasted with alumina particles at 350, 700 and 1000 kPa blasting pressure as depicted in Fig. 5, show almost a similar pattern as that of pristine samples (Fig.4(a)).

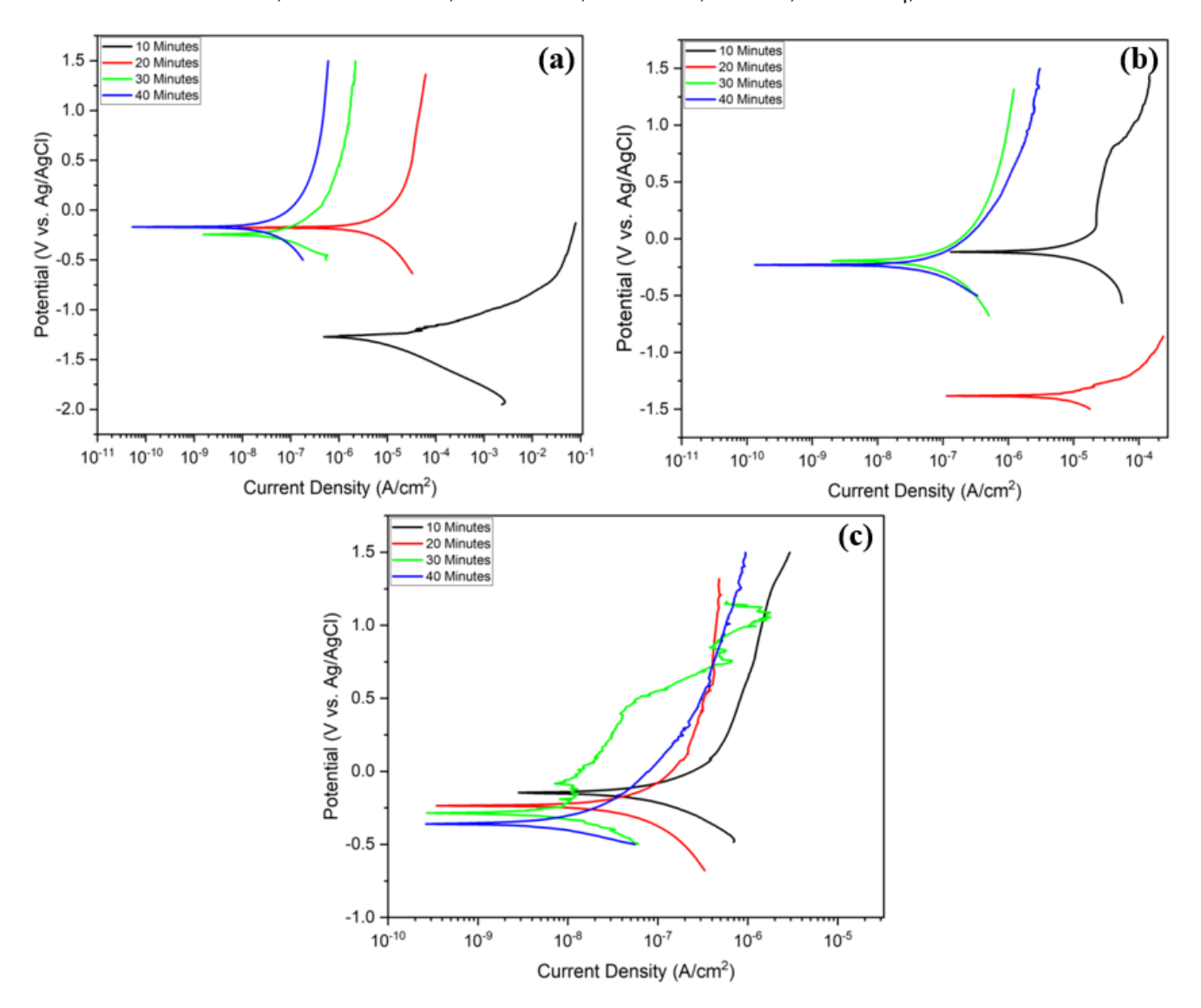


Figure 5: PD curves with different HA deposition times in SBF for Alumina blasted samples at a blasting pressure of (a) 350 kPa (b) 700 kPa (c) 1000 kPa.

It can be observed from the data presented in Table 6 that the values of Icorr decreased from 1.400 to $0.018 \,\mu\text{A/cm}^2$ and E_{corr} shifted from -1265.8 V to -169.9 V with an increase in HA deposition time. The near-tozero value of Icorr (0.0018 µA/cm²) confirms the full coverage in A350-HA40 sample compared to A350-HA10 sample (1.400 μA/cm²). Similarly, the R_p values (Table 6) show a 133-fold increase in polarization resistance from 27.77 to 3684.62 KΩcm² confirming the resistance behavior of the barrier film. Likewise, the values of corrosion rates (Table 6) show a 46-fold decrease from 3.93 to 0.085 mpy with an increase in HA deposition time which proves the efficiency of the barrier film. For the electrodeposited HA samples that were preblasted with alumina particles at a blasting pressure of 700 kPa, it is evident that the values of Icorr decreased from 0.871 to 0.009 µA/cm² and E_{corr} shifted from -103.9 V to -234.2 V with an increase in HA deposition duration. The almost zero value of I_{corr} (0.009 µA/cm²) indicates that A700-HA40 sample has achieved full coverage compared to A700-HA10 sample (0.871 μ A/cm²). Likewise, the corrosion rates values (Table 6) show a 404-fold decrease in corrosion rate from 2.83 to 0.007 with increase in anodization duration demonstrating the coating effectiveness. The R_p values (Table 6) show a 75-fold increase in polarization resistance from 66.80 to 5001.49 KΩcm² confirming the resistance characteristic of the barrier layer. For the electrodeposited HA samples that were pre-blasted with alumina particles at a blasting pressure of 1000 kPa, it observed can be that the values of I_{corr} decreased from 0.663 to 0.003 µA/cm² and E_{corr} shifted from -151.6 V to -357.9 V with an increase in HA deposition period. The nearly zero value of I_{corr} indicates that A1000-HA40 sample has achieved full coverage, as evidenced by the measured corrosion density of 0.003 μ A/cm² compared to A1000-HA10 sample (0.663 μ A/cm²). The values of corrosion rates (Table 6) exhibit a significant reduction of 492-fold, from

0.984 to 0.002 mpy, as the HA deposition period increases which clearly proves the efficiency of the barrier film. The R_p values (Table 6) demonstrate a 120-fold increase in polarization resistance, ranging from 82.35 to 9912.71 K Ω cm² which confirms the resistance characteristics of the barrier film.

Table 6: Electrochemical parameters selected for corrosion testing of Alumina blasted samples

		Electroc	hemical Parameters	
Sample	E _{corr} (mV)	I _{corr} (μΑ/cm²)	Corrosion Rate (mpy)	R _p (KΩcm²)
A350-HA10	-1265.8	1.400	3.93	27.77
A350-HA20	-173.1	0.690	1.65	64.04
A350-HA30	-253.0	0.353	0.695	148.89
A350-HA40	-169.9	0.018	0.085	3684.62
A700-HA10	-103.9	0.871	2.83	66.80
A700-HA20	-1387.2	0.676	0.952	88.98
A700-HA30	-191.6	0.145	0.381	408.78
A700-HA40	-234.2	0.009	0.007	5001.49
A1000-HA10	-151.6	0.663	0.984	82.35
A1000-HA20	-232.6	0.365	0.347	147.41
A1000-HA30	-278.9	0.064	0.125	695.79
A1000-HA40	-357.9	0.003	0.002	9912.71

3.3 Electrochemical Impedance Spectroscopy (EIS):

The results of electrochemical impedance spectroscopy, presented as a Nyquist plot and accompanying Bode plots, provide valuable insight of the characteristics of the HA layer formed on the surface. A depressed semicircle in the intermediate frequencies of a Nyquist plot indicates the capacitive nature of the HA layer. This capacitive loop's diameter demonstrates the magnitude of charge transfer resistance during corrosion/electrochemical reactions at the electrode surface across the coating in the test solution. The higher the impedance value (Z" value) and larger the diameter of the capacitive semicircle, greater will be the corrosion resistance [38]. Similarly, higher corrosion resistance is shown by a higher impedance value in the lower frequency region in the Bodeimpedance plot [39, 40]. The experimental EIS data can be analyzed by fitting an equivalent electrical circuit (EEC) to determine quantitative parameters such as

solution resistance (R_s), surface oxide film resistance (R_{ct}), charge transfer resistance (R_{ct}), and constant phase elements (CPEs). Constant phase elements (CPEs), namely the capacitance of the surface oxide film (CP_{Ef}) and the capacitance of the double layer (CPE_{dl}), are commonly used instead of pure capacitance to account for the heterogeneity of the electrode surface [41]. The impedance of a CPE (ZCPE) can be calculated by the formula as shown in Eq. 4 [42]: $Z_{CPE} = [Q(j\omega)^n]^{-1}$ (4)

Here, j = complex operator, ω = angular frequency, Q = magnitude of the CPE (related to its capacitance), n = exponent of the CPE [n=1 for an ideal capacitor, n=0.5 for diffusion-controlled electrodes, n=0 for an ideal resistor, intermediate values of n (0<n<1) are obtained for actual electrodes]. The equivalent electrical circuit (EEC), shown in Fig. 6, was used to fit on the EIS data of the electrodeposited HA samples. The fitted values of the circuit parameters are listed in Tables 7 – 9.

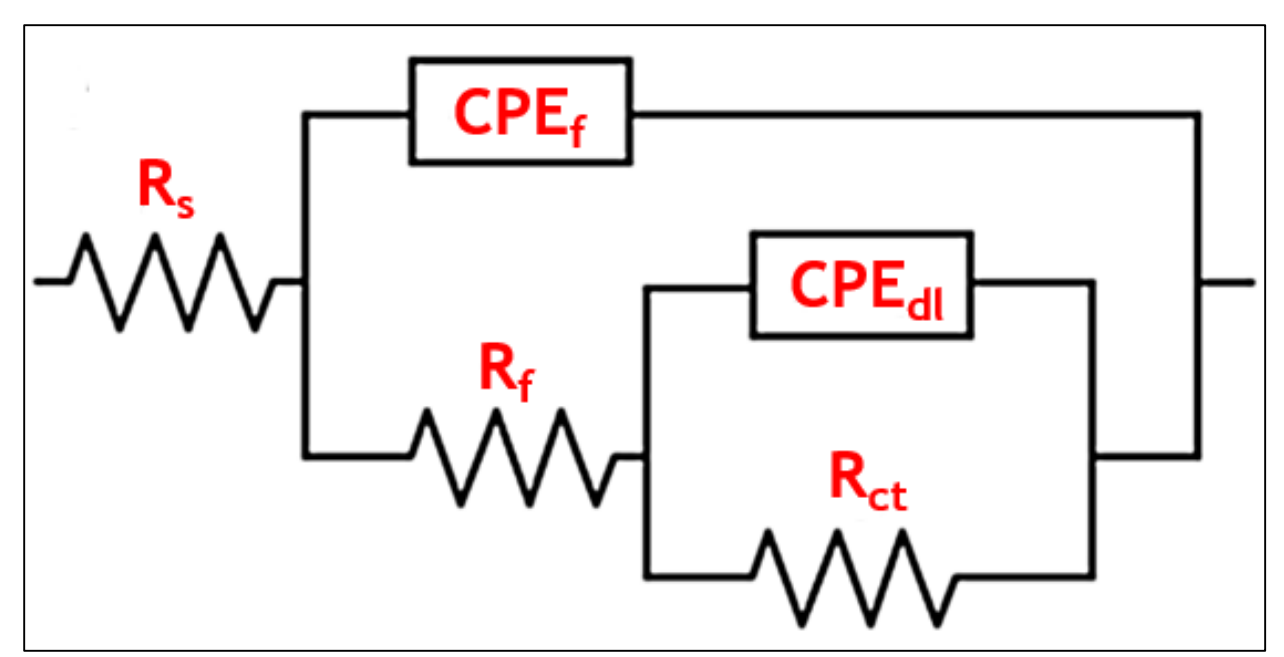


Figure 6: Equivalent Electrical Circuit (EEC) Model

The EIS results of pristine samples electrodeposited with HA coating for 10 to 40 minutes in SBF solution are shown in Fig. 7. The Nyquist plots (Fig. 7(a)) clearly show the capacitive behavior for all the coatings developed on all the samples.

However, the highest Z" value i.e. $3493~\Omega.cm^2$ and the large diameter of the depressed semicircles along the Z' axis for 40 minutes deposition time confirms the formation of HA layer with higher capacitance.

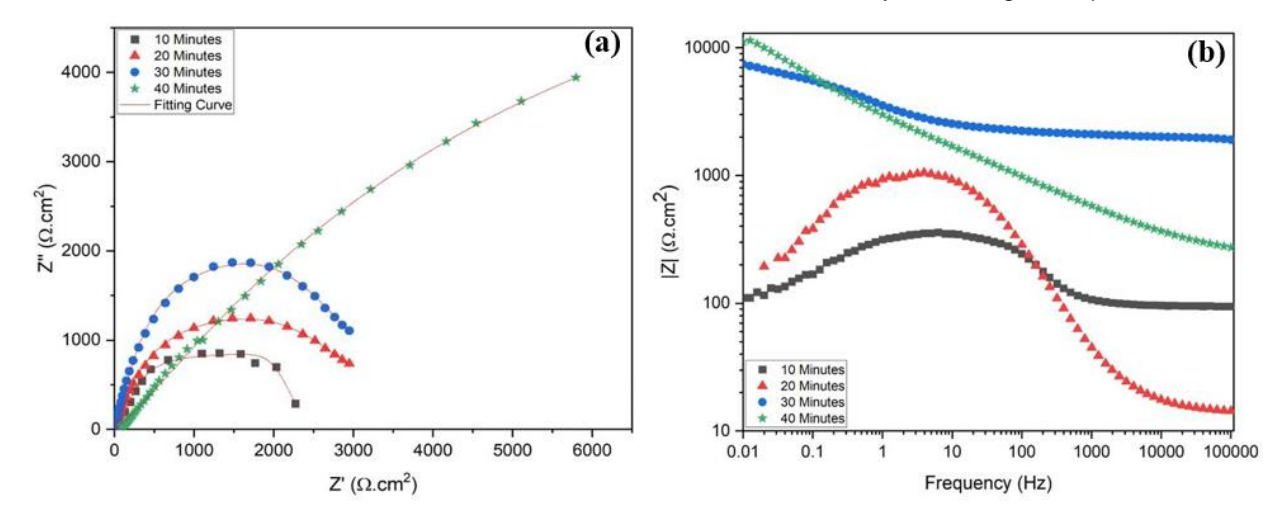


Figure 7: EIS of Pristine Samples with Different HA Deposition Times in SBF (a) Nyquist Plot (b) Bode-Impedance Modulus Plot

Similarly, the Bode-impedance modulus plot (Fig. 7(b)) shows the maximum value of 11390 Ω .cm² at lower frequency for PS-HA40 compared to others sample confirming the maximum corrosion resistance for this sample. The fitted values of the circuit parameters for

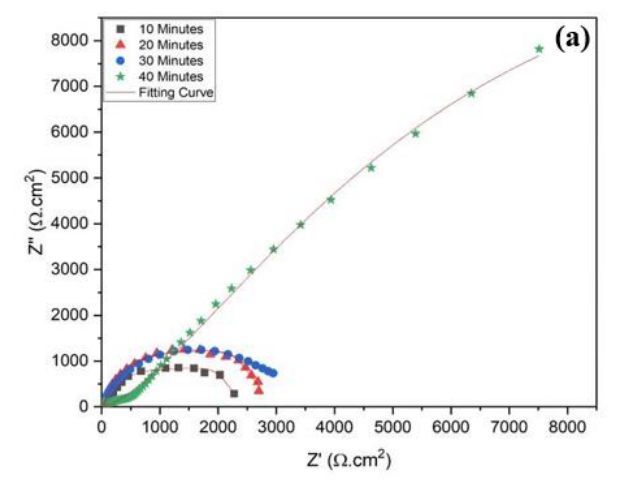
pristine samples electrodeposited with HA coating are shown in Table 7.

Table 7: Circuit Parameters of Pristine Samples with Different HA Coating Deposition Times

			Circuit Paramete	ers	
Sample	R_s (Ω .cm 2)	R _f (kΩ.cm²)	CPE _f (S.s ⁿ .cm ⁻²)	R_{ct} (k Ω .cm ²)	CPE _{dl} (S.s ⁿ .cm ⁻²)
PS-HA10	49.4	7.2	9.96E-5	16.1	11.85E-4
PS-HA20	44.8	9.4	9.07E-5	19.4	10.15E-4
PS-HA30	52.3	12.5	8.29E-5	25.3	9.32E-4
PS-HA40	48.5	15.1	6.19E-5	32.3	7.70E-4

The higher values of R_f (15.1 k Ω .cm²) and R_{ct} (32.3 k Ω .cm²) for PS-HA40 sample as compared to other samples confirms the protection nature of the HA layer. The higher values of R_{ct} than that of R_f for all HA deposition times confirm the formation of dense layer at the interface beneath the outer porous layer. Similarly, the decreasing trend of both CPE_{dl} and CPE_f with increasing HA deposition time is confirming the increase in compactness and pore free HA layer due to decrease in the effective area exposed to the electrolyte [43]. The EIS outcomes of HA electrodeposited samples preblasted with quartz particles at 350 kPa blasting pressure (Q350-HA10 – Q350-HA40) in SBF solution

are illustrated in Fig. 8. The capacitive behavior of all the HA electrodeposited samples is evident from the impedance values obtained from the Nyquist plot (Fig. 8(a)). However, the Z" value (7814 Ω .cm2) and the relatively larger diameter of the depressed semicircles along the Z' axis confirm that the Q350-HA40 sample has higher corrosion resistance compared to the other processed samples. Likewise, the Bode-impedance modulus plot (Fig. 8(b)) indicates a maximum value of 25620 Ω .cm² at lower frequency for Q350-HA40 sample as compared to other samples which confirms its maximum corrosion resistance.



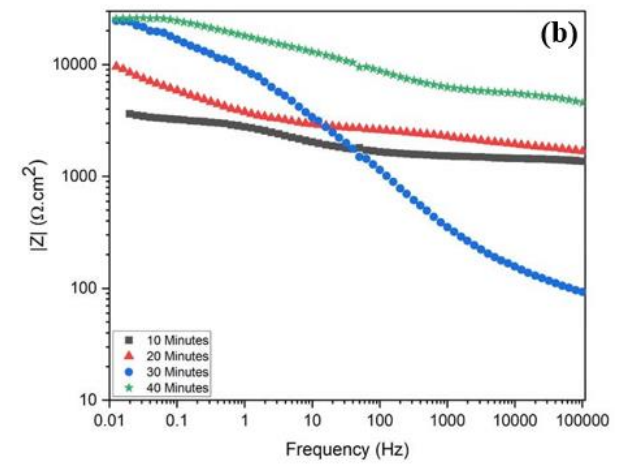


Figure 8: EIS of Quartz Blasted Samples at 350 kPa Blasting Pressure with Different HA Deposition Times in SBF (a) Nyquist Plot (b) Bode-Impedance Modulus Plot

The fitted values of the circuit parameters for Q350-HA10 – Q350-HA40 samples are displayed in Table 8. The higher values of $R_{\rm f}$ (17.2 $k\Omega.cm^2)$ and $R_{\rm ct}$ (37.2 $k\Omega.cm^2)$ for Q350-HA40 sample compared to other samples confirms the protective nature of the HA film. The higher values of $R_{\rm ct}$ compared to Rf for all HA deposition duration indicate the presence of dense layer at the interface beneath the outer porous layer. As the HA deposition duration increases, CPE_{dl} and CP_{Ef} tend

to decrease, which means that the less electrode surface is exposed to electrolyte due to compact and pore-free HA film. The EIS finding of HA electrodeposited samples pre-blasted with quartz particles at 700 kPa blasting pressure (Q700-HA10 – Q700-HA40) in SBF solution are displayed in Fig. 9. All the HA electrodeposited samples exhibit capacitive behavior, as seen by the impedance values from the Nyquist plot (Fig. 9(a)). The Z" value (9540 Ω.cm²)

and the diameter of the depressed semicircles along the Z' axis demonstrate that the Q700-HA40 sample has a

higher corrosion resistance compared to the other treated samples.

Table 8: Circuit parameters of Quartz blasted samples with different deposition times

			Circuit Paramete	ers	
Sample	R _s (Ω.cm²)	R _f (kΩ.cm²)	CPE _f (S.s ⁿ .cm ⁻²)	R_{ct} (k Ω .cm ²)	CPE _{dl} (S.s ⁿ .cm ⁻²)
Q350-HA10	48.1	8.7	9.56E-5	18.2	11.34E-4
Q350-HA20	38.3	10.3	8.47E-5	22.5	9.77E-4
Q350-HA30	50.1	14.4	6.37E-5	29.1	8.21E-4
Q350-HA40	45.5	17.2	5.68E-5	37.2	6.56E-4
Q700-HA10	49.2	10.4	8.09E-5	21.4	10.79E-4
Q700-HA20	41.3	12.8	7.76E-5	27.3	8.43E-4
Q700-HA30	54.5	17.3	5.32E-5	34.9	7.35E-4
Q700-HA40	56.2	19.9	3.12E-5	41.3	5.24E-4
Q1000-HA10	50.9	12.3	7.88E-5	24.5	8.66E-4
Q1000-HA20	45.7	15.4	6.43E-5	31.4	6.59E-4
Q1000-HA30	44.8	19.9	5.21E-5	39.6	6.70E-4
Q1000-HA40	53.2	20.2	2.99E-5	44.2	3.31E-4

Likewise, the Bode-impedance modulus plot (Fig. 9(b)) shows the value 44643.5 Ω .cm² at lower frequency for Q700-HA40 sample confirming the maximum corrosion resistance. The circuit parameter fitted values for Q700-

HA10 – Q700-HA40 samples are presented in Table 8. Rf (19.9 kΩ.cm²) and Rct (41.3 kΩ.cm²), which are the highest for the Q700-HA40 sample than that of other samples, prove that the HA layer is protective.

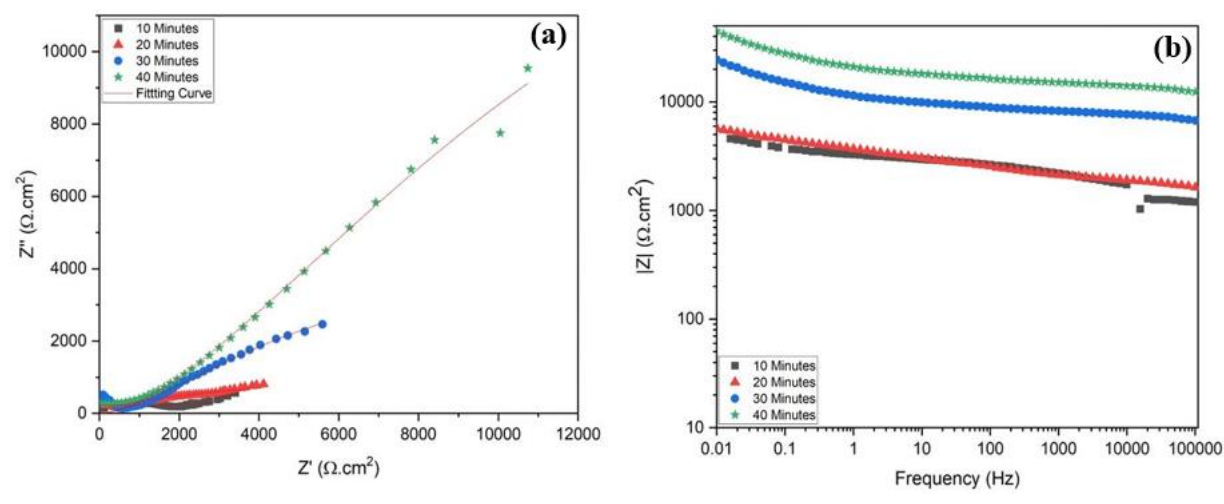


Figure 9: EIS of Quartz Blasted Samples at 700 kPa Blasting Pressure with Different HA Deposition Times in SBF (a) Nyquist Plot (b) Bode-Impedance Modulus Plot

Similarly, the higher values of R_{ct} compared to R_f for all HA deposition period and decrease in CPE_{dl} and CP_{Ef} with increase in HA deposition time is another evidence that the HA layer is compact and pore-free inner layer and porous outer layer with reduced effective area exposed to the electrolyte. The EIS studies of HA electrodeposited samples pre-blasted with quartz

particles at 1000 kPa blasting pressure (Q1000-HA10 – Q1000-HA40) in SBF solution are shown in Fig. 10. The Nyquist plot (Fig. 10(a)) clearly indicates the capacitive nature of all the HA electrodeposited samples based on the impedance values.

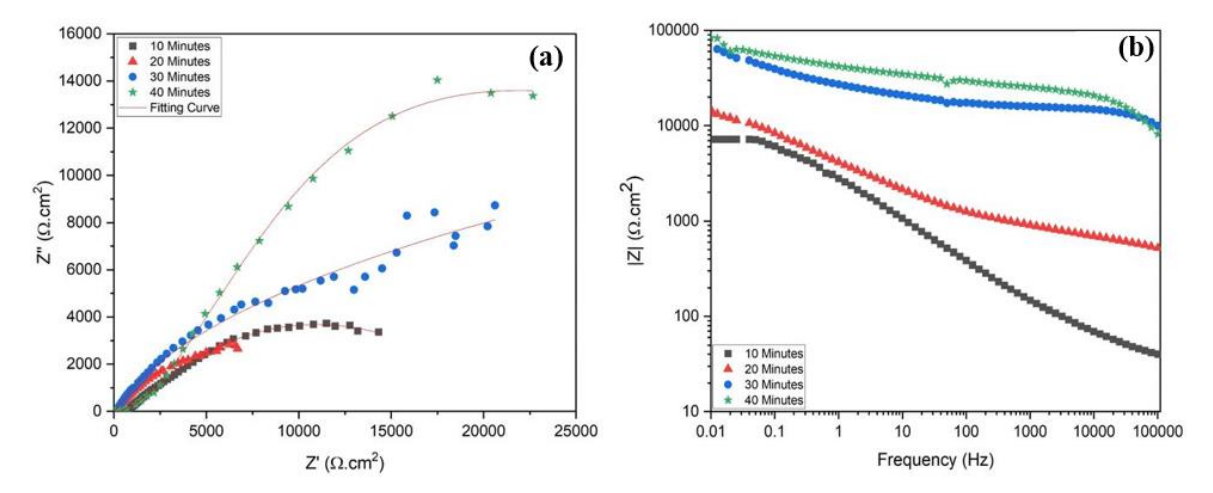


Figure 10: EIS of Quartz Blasted Samples at 1000 kPa Blasting Pressure with Different HA Deposition Times in SBF (a) Nyquist Plot (b) Bode-Impedance Modulus Plot

In contrast to the other treated samples, the Q1000-HA40 sample demonstrated maximum corrosion resistance, as confirmed by the highest Z" value of 14040 Ω .cm² and the maximum diameter of the depressed semicircles along the Z' axis. Likewise, the highest corrosion resistance for the Q1000-HA40 sample is confirmed by the Bode-impedance modulus plot, shown in Fig. 10(b), with the highest value of 83750 Ω .cm² at lower frequencies. The circuit parameter fitted values for Q1000-HA10 – Q1000-HA40 samples are provided in Table 8. The highest values of Rf (20.2 k Ω .cm²) and R_{ct} (44.2 k Ω .cm²) for the Q1000-HA40 sample, in comparison to other samples, provide

confirmation of the protective characteristics of the barrier layer. The observed decline in both CPE $_{dl}$ and CPE $_{fl}$ as HA deposition time increases provides further evidence of the compactness and pore-free barrier film resulting from a reduced surface area exposed to the electrolyte. Moreover, the higher values of R $_{ct}$ compared to R $_{fl}$ for all HA deposition time indicate the presence of a dense layer beneath the outer porous layer at the interface.

The EIS outcomes of HA electrodeposited samples preblasted with alumina particles at 350 kPa blasting pressure (A350-HA10 – A350-HA40) in SBF solution are illustrated in Fig. 11.

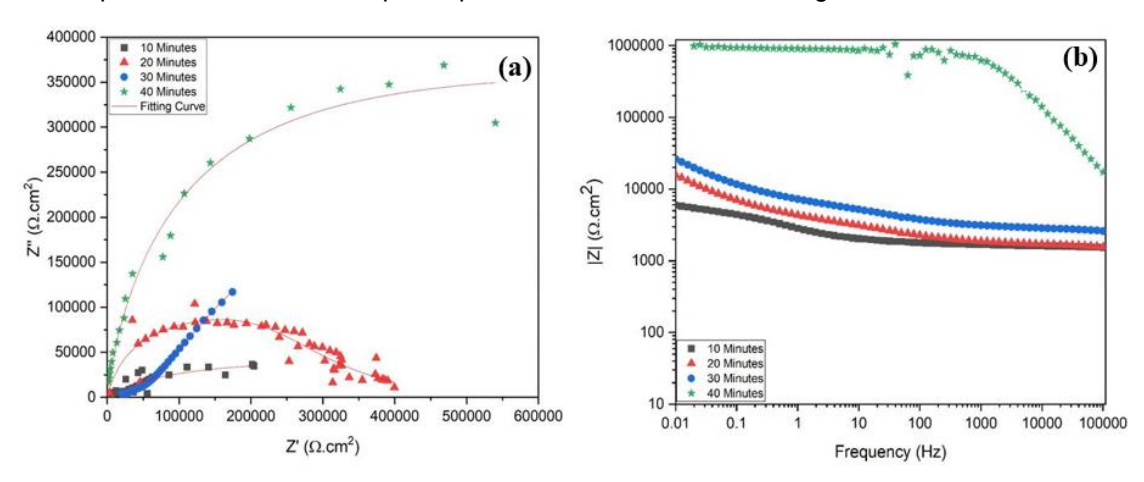


Figure 11: EIS of Alumina Blasted Samples at 350 kPa Blasting Pressure with Different HA Deposition Times in SBF (a) Nyquist Plot (b) Bode-Impedance Modulus Plot

The capacitive behavior of all the HA electrodeposited samples is evident from the impedance values obtained from the Nyquist plot (Fig. 11(a)). However, the highest Z'' value, which is 368900 Ω .cm², and the maximum

diameter of the depressed semicircles along the Z' axis confirm that the A350-HA40 sample has higher corrosion resistance compared to the other processed samples. The Bode-impedance modulus plot (Fig.

11(b)) indicates a maximum value of 982000 Ω .cm² at lower frequency for A350-HA40 sample which confirms its maximum corrosion resistance. The fitted values of

the circuit parameters for A350-HA10 – A350-HA40 are displayed in Table 9.

Table 9: Circuit Parameters of Alumina blasted samples with different deposition times

			Circuit Paramete	ers	
Sample	R _s (Ω.cm²)	R _f (kΩ.cm²)	CPE _f (S.s ⁿ .cm ⁻²)	R_{ct} (k Ω .cm ²)	CPE _{dl} (S.s ⁿ .cm ⁻²)
A350-HA10	49.1	24.5	10.52E-6	52.4	12.88E-3
A350-HA20	45.3	27.2	9.34E-6	56.9	11.76E-3
A350-HA30	51.6	29.5	7.39E-6	59.1	9.23E-3
A350-HA40	54.7	33.8	6.75E-6	64.8	8.20E-3
A700-HA10	51.2	26.2	9.18E-6	55.6	11.44E-3
A700-HA20	50.4	32.1	8.69E-6	60.2	9.78E-3
A700-HA30	53.5	37.4	6.55E-6	63.2	8.97E-3
A700-HA40	51.2	41.2	5.28E-6	67.1	7.67E-3
A1000-HA10	44.3	36.2	8.27E-6	59.2	10.22E-3
A1000-HA20	56.8	41.3	7.56E-6	64.5	9.95E-3
A1000-HA30	59.2	43.9	6.98E-6	68.4	7.67E-3
A1000-HA40	49.1	46.4	4.32E-6	72.3	5.21E-3

The highest values of Rf (33.8 k Ω .cm²) and R_{ct} (64.8 k Ω .cm²) for A350-HA40 sample compared to other samples confirms the protective nature of the HA film. As the HA deposition duration increases, CPE_{dl} and CPE_f tend to decrease, which means that the electrolyte is exposed to less of the film, leading to a more compact and pore-free HA film. Likewise, the higher values of R_{ct}

compared to Rf for all HA deposition duration indicate the presence of dense layer at the interface beneath the outer porous layer. The EIS results of HA electrodeposited samples pre-blasted with alumina particles at 700 kPa blasting pressure (A700-HA10 – A700-HA40) in SBF solution are displayed in Fig. 12.

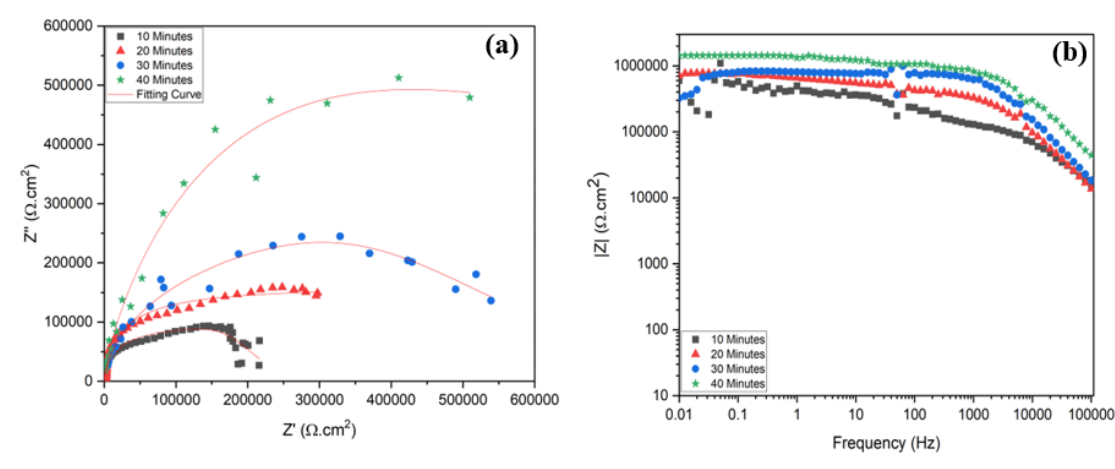


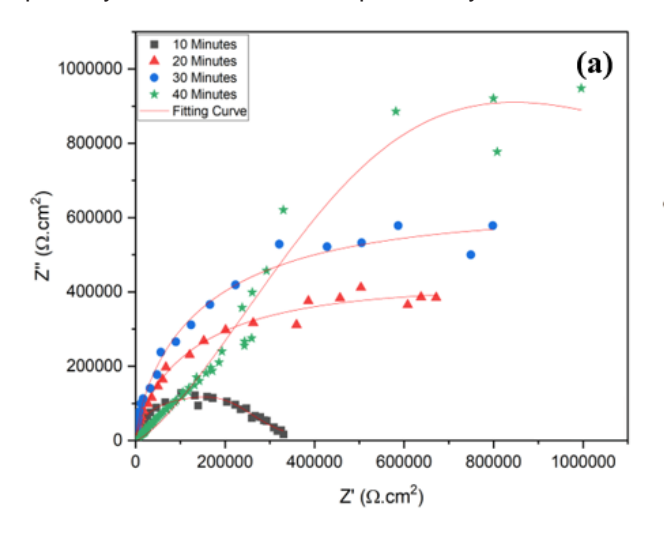
Figure 12: EIS of Alumina Blasted Samples at 700 kPa Blasting Pressure with Different HA Deposition Times in SBF (a) Nyquist Plot (b) Bode-Impedance Modulus Plot

All the HA electrodeposited samples exhibit capacitive behavior, as seen by the impedance values from the Nyquist plot (Fig. 12(a)). The Z" value, which is 512600 Ω .cm², and the diameter of the depressed semicircles along the Z' axis

demonstrate that the A700-HA40 sample has a higher corrosion resistance compared to the other treated samples. Likewise, the Bode-impedance modulus plot (Fig. 12(b)) shows the value 1430560 Ω .cm² at lower frequency for A700-HA40 sample

confirming the maximum corrosion resistance. The circuit parameter fitted values for A700-HA10 – A700-HA40 samples are presented in Table 9. R_f (41.2 k Ω .cm²) and R_{ct} (67.1 k Ω .cm²), which are the highest for the A700-HA40 sample than that of other samples, prove that the HA layer is protective. The higher values of R_{ct} compared to Rf for all HA deposition period indicate the presence of a compact layer beneath the outer porous layer at the

interface. The fact that CPE_{dl} and CPE_f tend to decrease as the HA deposition time increases is another evidence that the HA layer is compact and pore-free due to the reduced effective area exposed to the electrolyte. The EIS outcomes of HA electrodeposited samples pre-blasted with alumina particles at 1000 kPa blasting pressure (A1000-HA10- A1000-HA40) in SBF solution are depicted in Fig. 13.



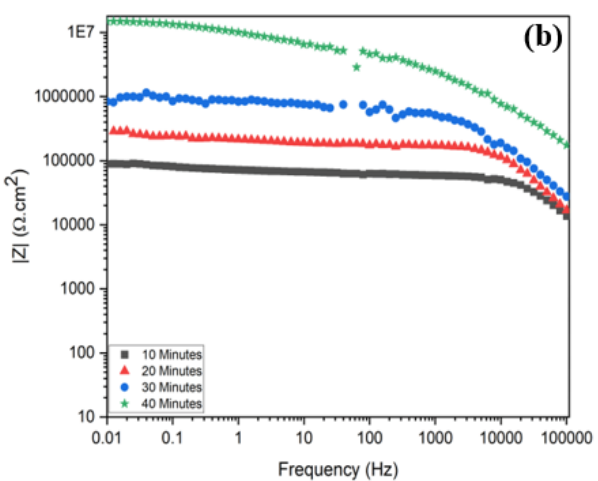


Figure 13: EIS of Alumina Blasted Samples at 1000 kPa Blasting Pressure with Different HA Deposition Times in SBF (a) Nyquist Plot (b) Bode-Impedance Modulus Plot

The Nyquist plot (Fig. 13(a)) clearly indicates the capacitive nature of all the HA electrodeposited samples based on the impedance values. In contrast to the other treated samples, the A1000-HAT40 sample demonstrated maximum corrosion resistance, as confirmed by the highest Z" value of 948000 Ω .cm² and the maximum diameter of the depressed semicircles along the Z' axis. Likewise, the highest corrosion resistance for the A1000-HA40 sample is confirmed by the Bode-impedance modulus plot, shown in Fig. 13(b) at lower frequencies, with a value of 14913000 Ω .cm². The circuit parameter fitted values for A1000-AT10 -A1000-AT40 samples are provided in Table 9. The higher values of Rf (46.4 kΩ.cm²) and Rct (72.3 $k\Omega$.cm²) for the A1000-HA40 sample, in comparison to other samples, provide confirmation of the protective characteristics of the barrier layer. CPEd and CPEf tend to decrease as the HA deposition duration increases, which means that the electrolyte is exposed to less of the film, leading to a more compact and pore-free HA film. Likewise, the higher Rct values compared to Rf for all HA deposition duration indicate the presence of dense layer at the interface beneath the outer porous layer.

Conclusions:

The findings from the potentiodynamic polarization scans conducted on the pristine, quartz, and alumina blasted samples at various blasting pressures indicate that both blasting pressure and blasting media play an essential role in the development of the hydroxyapatite layer along with the processing time. The alumina blasted surface demonstrates the development of a hydroxyapatite layer which indicates improved corrosion resistance and polarization resistance. The increase in processing time results in a better hydroxyapatite layer with full surface coverage. Similarly, the EIS data confirms the capacitance characteristics of the compact and pore-free inner layer with porous outer layer, observed in the samples subjected to a blasting pressure of 1000 kPa for a deposition time minutes. The development of hydroxyapatite layer on alumina blasted samples is superior compared to quartz blasted samples.

References:

- [1]. F. Witte et al., "In vitro and in vivo corrosion measurements of magnesium alloys," Biomater., vol. 27, pp. 1013-1018, Mar. 2006.
- [2] L. Xu et al., "In vitro and in vivo evaluation of the surface bioactivity of a calcium phosphate coated magnesium alloy," Biomater., vol. 30, pp. 1512-1523, Mar. 2009.
- [3] B. Li and Y. Han, "Fast formation of a novel bilayer coating with enhanced corrosion resistance and cytocompatibility on magnesium," RSC Adv., vol. 5, pp. 46109-46118, May 2015.
- [4] L. Chang, L. Tian, W. Liu, and X. Duan, "Formation of dicalcium phosphate dihydrate on magnesium alloy by micro-arc oxidation coupled with hydrothermal treatment," Corros. Sci., vol. 72, pp. 118- 124, Jul. 2013.
- [5] L.-Y. Cui et al., "In vitro corrosion of Mg–Ca alloy - The influence of glucose content," Front. Mater. Sci., vol. 11, pp. 284-295, Aug. 2017.
- [6] L. Mao et al., "Enhanced bioactivity of Mg-Nd-Zn-Zr alloy achieved with nanoscale MgF2 surface for vascular stent application," ACS Appl. Mater. Interfaces, vol. 7, pp. 5320-5330, Feb. 2015.
- [7] M. A. Khan et al., "Evolution of microstructure, texture, and mechanical performance of Mg-13Gd-2Er-0.3 Zr alloy by double extrusion at different temperatures," Arch. Civ. Mech. Eng. 25, 26(2025).
- [8] F. Peng et al., "Enhanced corrosion resistance and biocompatibility of magnesium alloy by Mg-Al-layered double hydroxide," ACS Appl. Mater. Interfaces, vol. 8, pp. 35033-35044, Dec. 2016.
- [9] S. Yoshizawa, A. Brown, A. Barchowsky, and C. Sfeir, "Magnesium ion stimulation of bone marrow stromal cells enhances osteogenic activity, simulating the effect of magnesium alloy degradation," Acta Biomater., vol. 10, pp. 2834-2842, Jun. 2014.
- [10] S. Chen et al., "In vivo study on degradation behavior and histologic response of pure magnesium in muscles," J. Mater. Res.

- Technol., vol. 33, pp. 469-474, May 2017.
- [11] L. Tan et al., "Loss of mechanical properties in vivo and bone-implant interface strength of AZ31B magnesium alloy screws with Sicontaining coating," Acta Biomater., vol. 10, pp. 2333-2340, May 2014.
- [12] P. Wan, L. Tan, and K. Yang, "Surface modification on biodegradable magnesium alloys as orthopedic implant materials to improve the bio-adaptability: A review," J. Mater. Res. Technol., vol. 32, pp. 827–834, Sep. 2016.
- [13] G. Wu, J.M. Ibrahim, and P.K. Chu, "Surface design of biodegradable magnesium alloys

 A review," Surf. Coat. Technol., vol. 233, pp. 2-12, Oct. 2013.
- [14] K. Catt, H. Li, and X. T. Cui, "Poly (3,4-ethylenedioxythiophene) graphene oxide composite coatings for controlling magnesium implant corrosion," Acta Biomater., vol. 48, pp. 530-540, Jan. 2017.
- [15] J. de O. Braga et al., "Fabrication and characterization of dicalcium phosphate coatings deposited on magnesium substrates by a chemical conversion route," Surf. Coat. Technol., vol. 38, p. 125505, Mar. 2020.
- [16] G. Song, "Control of biodegradation of biocompatible magnesium alloys," Corros. Sci., vol. 49, pp. 1696-1701, Apr. 2007.
- [17] F. Hussain et al., "Optimizing Biocompatibility of Mg-AZ31B Alloy through Varied Surface Roughness and Anodization Time," Iranian J. Mat. Sci. Eng., vol. 21, No. 3, Sep.2024.
- [18] F. Hussain et al., "The Effect of Surface Roughness and Deposition Time on the Biocompatibility of Electrodeposited Hydroxyapatite Coating on Grit-Blasted AZ31B Mg Alloy," Iranian J. Sci. 2024.
- [19] S. S. A. El-Rahman, "Neuropathology of aluminum toxicity in rats (glutamate and GABA impairment)," Pharmacol. Res., vol. 47, pp. 189-194, Mar. 2003.
- [20] Y. Nakamura, Y. Tsumura, Y. Tonogai, T. Shibata, and Y. Ito, "Differences in behavior among the chlorides of seven rare earth elements administered intravenously to rats,

- Fundam. Appl. Toxicol., vol. 37, pp. 106-116, Jun. 1997.
- [21] Y. Weidong, Z. Ping, L. Jiesheng, and X. Yanfang, "Effect of Long-Term Intake of Y3+ in Drinking Water on Gene Expression in Brains of Rats," J. Rare Earths, vol. 24, pp. 369-373, Jun. 2006.
- [22] M. Jamesh, S. Kumar, and T. S. N. S. Narayanan, "Electrodeposition of hydroxyapatite coating on magnesium for biomedical applications," J. Coat. Technol. Res., vol. 9, pp. 495-502, Dec. 2011.
- [23] H. Hornberger, S. Virtanen, and A.R. Boccaccini, "Biomedical coatings on magnesium alloys A review," Acta Biomater., vol. 8, pp. 2442-2455, Jul. 2012.
- [24] Y. Su et al., "Enhancing the corrosion resistance and surface bioactivity of a calciumphosphate coating on a biodegradable AZ60 magnesium alloy via a simple fluorine posttreatment method," RSC Adv., vol. 5, pp. 56001-56010, Jun. 2015.
- [25] C. Prakash, S. Singh, B.S. Pabla, and M.S. Uddin, "Synthesis, characterization, corrosion and bioactivity investigation of nano-HA coating deposited on biodegradable Mg-Zn-Mn alloy," Surf. Coat. Technol., vol. 346, pp. 9-18, Jul. 2018.
- [26] Y. C. Su et al., "Improving the degradation resistance and surface biomineralization ability of calcium phosphate coatings on a biodegradable magnesium alloy via a sol-gel spin coating method," J. Electrochem. Soc., vol. 165, pp. C155-C161, Mar. 2018.
- [27] Y. T. Guo et al., "Enhanced corrosion resistance and biocompatibility of biodegradable magnesium alloy modified by calcium phosphate/collagen coating," Surf. Coat. Technol., vol. 401, p. 126318, Nov. 2020.
- [28] T. J. Liu et al., "A biodegradable, mechanically tunable micro-arc oxidation AZ91D-based composite implant with calcium phosphate/chitosan coating promotes long-term bone tissue regeneration," Biotechnol. J., vol. 16, p. 2000653, Oct. 2021.
- [29] A. Ali et al., "Hydrothermal deposition of high

- strength calcium phosphate coatings on magnesium alloy for biomedical applications," Surf. Coat. Technol., vol. 357, pp. 716-727, Jan. 2019.
- [30] W. Zai, S. Sun, H. C. Man, J. S. Lian, and Y. S. Zhang, "Preparation and anticorrosion properties of electrodeposited calcium phosphate (CaP) coatings on Mg–Zn–Ca metallic glass," Mater. Chem. Phys., vol. 290, p. 126532, Oct. 2022.
- [31] M. Horynová et al., "Design of tailored biodegradable implants: the effect of voltage on electrodeposited calcium phosphate coatings on pure magnesium," J. Am. Ceram. Soc., vol. 102, pp. 123-135, Jan. 2019.
- [32] M. Uddin, C. Hall, and V. Santos, "Fabrication, characterisation and corrosion of HA coated AZ31B Mg implant material: effect of electrodeposition current density," Surf. Coat. Technol., vol. 385, p. 125363, Mar. 2020.
- [33] H. R. Bakhsheshi-Rad, E. Hamzah, S.N. Saud, and M. Medraj, "Effect of electrodeposition parameters on the microstructure and corrosion behavior of DCPD coatings on biodegradable Mg-Ca-Zn alloy," Int. J. Appl. Ceram. Technol., vol. 12, pp. 1054-1064, Oct. 2015.
- [34] W. Lu et al., "Microstructure and in vitro corrosion properties of ZK60 magnesium alloy coated with calcium phosphate by electrodeposition at different temperatures," Int. J. Electrochem. Sci., vol. 8, pp. 10746-10757, Aug. 2013.
- [35] H. Wang et al., "Formation mechanism of Cadeficient hydroxyapatite coating on Mg–Zn–Ca alloy for orthopaedic implant," Appl. Surf. Sci., vol. 307, pp. 92-100, Jul. 2014.
- [36] H. X. Wang, S.K. Guan, X. Wang, C.X. Ren, and L.G. Wang, "In vitro degradation and mechanical integrity of Mg–Zn–Ca alloy coated with Ca-deficient hydroxyapatite by the pulse electrodeposition process," Acta Biomater., vol. 6, pp. 1743-1748, May 2010.
- [37] F. Hussain, M. U. Manzoor, M. Kamran, and M. T. Z., "The effect of grit blasting on surface roughness and hardness of magnesium Alloy

- AZ31B: A statistical study," Phys. Met. Metallogr., vol. 124, pp. 1620-1631, Dec. 2023.
- [38] T. Sridhar, U. K. Mudali, and M. Subbaiyan, "Preparation and characterization of electrophoretically deposited hydroxyapatite coatings on type 316L stainless steel," Corros.Sci., vol. 45, pp 237-252, Feb. 2003.
- [39] B. L. Luan, D. Yang, X. Y. Liu, and G. L. Song, "Corrosion protection of magnesium (Mg) alloys using conversion and electrophoretic coatings," Corrosion of Magnesium Alloy, vol. 2, pp. 541-564, 2011.
- [40] X. Cui et al., "Corrosion behaviors in physiological solution of cerium conversion coatings on AZ31 magnesium alloy," Appl. Surf. Sci., vol. 257, pp. 9703-9709, Sep. 2011.
- [41] B. M. Fernandez-Perez, J. A. Gonzalez-Guzman, S. Gonzalez, and R. M. Souto, "Electrochemical impedance spectroscopy investigation of the corrosion resistance of a waterborne acrylic coating containing active electrochemical pigments for the protection of carbon steel," Int. J. Electrochem. Sci., vol. 9, pp. 2067- 2079, Apr. 2014.
- [42] W. C. Say, C. C. Chen, and S. J. Hsieh, "Electrochemical characterization of nonchromate surface treatments on AZ80 magnesium," Mater. Charact., vol. 59, pp. 1400-1406, Oct. 2008.
- [43] M. Babaei, C. Dehghanian, and M. Vanaki, "Effect of additive on electrochemical corrosion properties of plasma electrolytic oxidation coatings formed on CP Ti under different processing frequency," Appl. Surf. Sci., vol. 357A, pp. 712-720, Dec. 2015.
- [44] L. Zhang et al., "Study on the anodic film formation process of AZ91D magnesium alloy," Electrochim. Acta, 2007, vol. 52, pp. 5325-5333, May 2007.
- [45] I. G. Ogunsanya and C. M. Hansson, "The semiconductor properties of passive films and corrosion behavior of stainless steel reinforcing bars in simulated concrete pore solution," Mater., vol. 6, p. 100321, Jun. 2019.
- [46] M. Santamaria, G. Tranchida, and F. Di

Franco, "Corrosion resistance of passive films on different stainless steel grades in food and beverage industry," Corros. Sci., vol. 173, p. 108778, Aug. 2020.